

Observation of multiple flat bands and topological Dirac states in a new titanium based slightly distorted kagome metal YbTi_3Bi_4

Anup Pradhan Sakhya,^{1,*} Brenden R. Ortiz,^{2,*} Barun Ghosh,³ Milo Sprague,¹ Mazharul Islam Mondal,¹ Matthew Matzelle,³ Iftakhar Bin Elius,¹ Nathan Valadez,¹ David G. Mandrus,^{4,5,6} Arun Bansil,³ and Madhab Neupane^{1,†}

¹*Department of Physics, University of Central Florida, Orlando, Florida 32816, USA*

²*Materials Science and Technology Division, Oak Ridge National Laboratory, Oak Ridge, Tennessee 37830, USA*

³*Department of Physics, Northeastern University, Boston, Massachusetts 02115, USA*

⁴*Department of Materials Science and Engineering,*

The University of Tennessee, Knoxville, Tennessee 37996, USA

⁵*Department of Physics and Astronomy, University of Tennessee Knoxville, Knoxville, Tennessee 37996, USA*

⁶*Materials Science and Technology Division, Oak Ridge National Laboratory, Oak Ridge, Tennessee 37831, USA*

(Dated: September 6, 2023)

Kagome lattices have emerged as an ideal platform for exploring various exotic quantum phenomena such as correlated topological phases, frustrated lattice geometry, unconventional charge density wave orders, Chern quantum phases, superconductivity etc. In particular, the vanadium based nonmagnetic kagome metals AV_3Sb_5 ($A = \text{K}, \text{Rb}, \text{and Cs}$) have seen a flurry of research interest due to the discovery of multiple competing orders. Here, we report the discovery of a new Ti based kagome metal YbTi_3Bi_4 and employ angle-resolved photoemission spectroscopy (ARPES), magnetotransport in combination with density functional theory calculations to investigate its electronic structure. We reveal spectroscopic evidence of multiple flat bands arising from the kagome lattice of Ti with predominant Ti $3d$ character. Through our calculations of the Z_2 indices, we have identified that the system exhibits topological nontriviality with surface Dirac cones at the $\bar{\Gamma}$ point and a quasi two-dimensional Dirac state at the \bar{K} point which is further confirmed by our ARPES measured band dispersion. These results establish YbTi_3Bi_4 as a novel platform for exploring the intersection of nontrivial topology, and electron correlation effects in this newly discovered Ti based kagome lattice.

I. INTRODUCTION

The kagome lattice, composed of two-dimensional honeycomb network of alternating corner-sharing triangles have attracted enormous research interest recently as they provide a fascinating platform for the emergence of multiple novel topological and correlated electronic phenomena [1–3]. Due to the kagome geometry, it possesses intriguing features such as the presence of flat bands, Dirac fermions, and van Hove singularities thus resulting in a complex interplay between geometry, topology, and electron correlations [4–18]. In the past few years, there have been notable discoveries of various exotic phenomena in several kagome magnets, such as Fe_3Sn_2 exhibiting massive Dirac fermions [7], antiferromagnets Mn_3Sn and Mn_3Ge showcasing giant anomalous Hall effect [19, 20] and the discovery of Weyl semimetal state in a magnetic kagome material $\text{Co}_3\text{Sn}_2\text{S}_2$ [21, 22].

The RMn_6Sn_6 family ($R =$ rare earth elements, and the kagome layers are formed by manganese atoms) has garnered considerable attention in recent times as they exhibit unique magnetic tunability and large Berry curvature fields [10, 14, 23–32]. In particular, TbMn_6Sn_6 hosts massive Dirac fermions at the K point owing to the observation of Landau quantization and the presence of Landau fan diagram [10, 23]. Flat bands and

Dirac fermions have been reported in RMn_6Sn_6 ($R = \text{Gd}, \text{Dy}, \text{Y}$) [14, 24, 25], topological Hall effect have been observed in YMn_6Sn_6 , ErMn_6Sn_6 , HoMn_6Sn_6 [28–31], and large anomalous Hall effect has been reported in LiMn_6Sn_6 [33]. In addition to these extensively investigated magnetic kagome materials, a new class of kagome superconductors AV_3Sb_5 ($A = \text{K}, \text{Rb}, \text{and Cs}$) were discovered and found to host nontrivial band topology, charge density wave order and superconducting ground state [34–43]. Recently, two new kagome metals, YbV_3Sb_4 and EuV_3Sb_4 were reported, introducing a new family of Vanadium-based kagome materials [44]. It was found that YbV_3Sb_4 is a Pauli paramagnet with no clear thermodynamic phase transition between 300 K and 60 mK whereas EuV_3Sb_4 displays a ferromagnetic transition below T_c of roughly 32 K and signature of spin-texture in low-field. In contrast to the vanadium based kagome lattices, reports on the isostructural titanium-based kagome materials are still rare. LaTi_3Bi_4 , CeTi_3Bi_4 , and EuTi_3Bi_4 have been reported [45] but comprehensive investigations are limited.

Here, we have performed a comprehensive investigation of the electronic structure of the newly discovered YbTi_3Bi_4 kagome material. Our approach involved the use of magneto-transport measurements, angle-resolved photoemission spectroscopy (ARPES), and density-functional theory (DFT) calculations. Our X-ray diffraction measurements demonstrate this material crystallizes in the orthorhombic $Fmmm$ space group [46]. Similar to the V-Sb analog YbV_3Sb_4 ,

* These authors contributed equally in this work.

† Corresponding author: madhab.neupane@ucf.edu

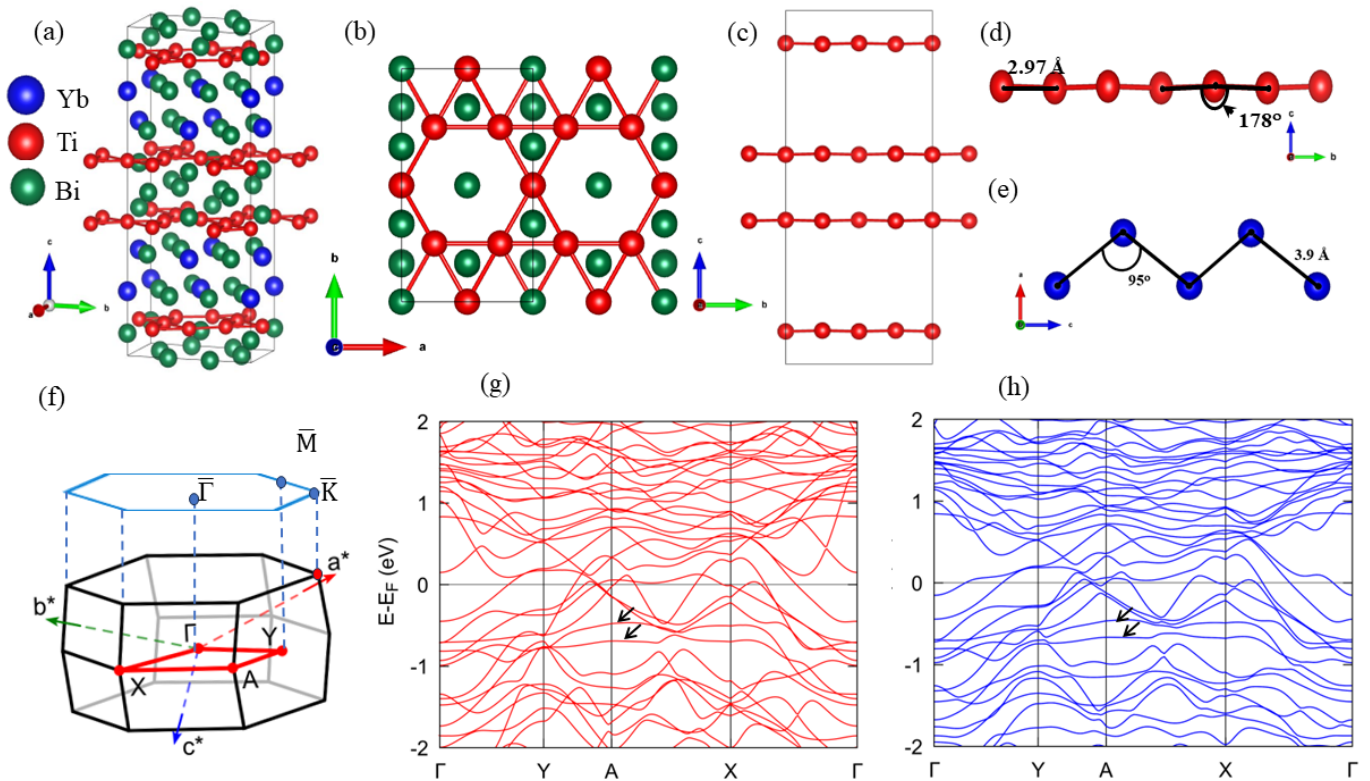


Fig. 1. Crystal structure and DFT calculations of YbTi_3Bi_4 . (a) Crystal structure of YbTi_3Bi_4 where the blue, red, and green colored solid spheres denote the Yb, Ti and Bi atoms, respectively. The crystal structure is orthorhombic ($Fm\bar{3}m$) with a zigzag sublattice of Yb atoms. (b) The kagome lattice is formed by Ti atoms, (c) which is slightly distorted and not coplanar. (d) The distortion is relatively small ($\sim 2^\circ$). (e) the zig-zag chain formed by Yb atoms. (f) Bulk Brillouin zone (BZ) and its projection on to the (001) surface BZ. High symmetry points are marked. (g) DFT calculations along the various high-symmetry directions without the inclusion of spin-orbit coupling (SOC). (h) DFT calculations along the various high-symmetry directions with the inclusion of SOC.

YbTi_3Bi_4 is decidedly nonmagnetic due to the divalent Yb^{2+} . No transitions were observed in magnetization measurements down to 60 mK. Our ARPES measurements reveal the presence of multiple flat bands in this material along with the presence of linear Dirac states at the center of the Brillouin zone (BZ) i.e., at the $\bar{\Gamma}$ point and at the corner of the BZ i.e., the \bar{K} point. The obtained ARPES results are reproduced from DFT calculations. Our observation of multiple flat bands and Dirac states in YbTi_3Bi_4 establishes this material as a fertile system for exploring the interplay between kagome geometry, non-trivial band topology and electron correlation in an easily exfoliable new Ti-based nonmagnetic kagome material. The present study highlights the importance of this newly discovered LnTi_3Bi_4 kagome family as a new platform to explore the influence of magnetism, spin-orbit coupling, and electron correlations as one can easily replace the Yb rare earth element by other magnetic rare earth elements [46].

II. EXPERIMENTAL AND COMPUTATIONAL DETAILS

YbTi_3Bi_4 single crystals are grown through a bismuth self-flux. Elemental reagents of Yb (Alfa 99.9%), Ti (Alfa 99.9% powder), and Bi (Alfa 99.999% low-oxide shot) were combined at a 2:3:12 ratio into 2 mL Canfield crucibles fitted with a catch crucible and a porous frit [47]. The crucibles were sealed under approximately 0.7 atm of argon gas in fused silica ampoules. Each composition was heated to 1050 °C at a rate of 200 °C/hr. Samples were allowed to thermalize and homogenize at 1050 °C for 12-18 h before cooling to 500 °C at a rate of 2 degree C/hr. Excess bismuth was removed through centrifugation at 500 °C. The synchrotron-based ARPES experiments were performed at the ALS beamlines 10.0.1.1 and 4.0.3 equipped with a R4000 and R8000 hemispherical electron analyzer. The angular and energy resolution were set at better than 0.2 ° and 15 meV, respectively. High-quality single crystals were cut into small pieces and mounted on a copper post using a Torr seal. Ceramic posts were attached on top of the samples. To avoid any oxidation, the sample preparation was performed inside a glove box. The samples were then loaded into the main chamber which was cooled and pumped down for a few hours. The measurements were carried out at a

temperature of 11 K. The pressure in the UHV chamber was maintained in the order of 10^{-11} Torr. All the electronic structure calculations were performed within the density functional theory (DFT) framework using a plane wave basis set as implemented in the Vienna Ab initio Simulation Package (VASP) [48, 49]. The standard projector-augmented-wave (PAW) pseudopotentials were used [50]. The kinetic energy cutoff for the plane wave basis was set to 500 eV. A Gamma-centered $10 \times 10 \times 10$ k -mesh was used for the k -space integration. The SCAN (strongly constrained and appropriately normed) functional was adopted to treat the correlation effects properly [51, 52]. The DFT calculations were performed by fully relaxing the lattice parameters and the atomic positions until the force on each atom became less than 0.001 eVÅ. The relaxed lattice parameters are $a=5.862$ Å, $b=10.385$ Å, $c=24.838$ Å, which are very close to the experimental values.

III. RESULTS AND DISCUSSION

YbTi_3Bi_4 has a layered crystal structure and crystallizes in the orthorhombic space group $Fmmm$ (No. 69) with $a = 5.91(4)$ Å, $b = 10.3(4)$ Å, $c = 24.9(4)$ Å, and $\alpha = \beta = \gamma = 90^\circ$. As shown in Fig. 1(a,b), the crystal structure consists of Ti kagome layers stacked along the b -axis between Bi and Yb atoms. To emphasize the kagome lattice formed by Ti atoms, we have intentionally removed the Ti-Bi, Yb-Ti, and Yb-Yb bonds in our discussion. The kagome layers formed by Ti atoms can be better visualized in Fig. 1(b), where each unit cell consists of four kagome layers. However, unlike the AV_3Sb_5 compounds, the kagome layers formed by Ti atoms in YbTi_3Bi_4 exhibit a slight buckling [see Fig. 1(c,d)], indicating a slight distortion in the Ti kagome layers. Additionally, the distance between Ti atoms (Ti-Ti) are not equivalent. Fig. 1e illustrates the zigzag chains formed by Yb atoms extending in the a -direction. The Yb-Yb distance within the chain measures approximately 3.9 Å, which is significantly shorter compared to the nearest neighbor Yb-Yb interchain distance, which spans approximately 5.7 Å.

Turning to the electronic structure, the bulk Brillouin zone (BZ) of YbTi_3Bi_4 and its projection on the (001) surface is shown in Fig. 1(f). Note that DFT calculation suggests that the density of states at the Fermi level is dominated by Ti and Bi-based orbitals. With the Yb-orbitals a bit further away, the ARPES is expected to show an apparent 6-fold symmetry, though the underlying structure remains orthorhombic. As such, we show the projection on the (001) labeled with the pseudo-hexagonal \bar{M} , \bar{K} , $\bar{\Gamma}$ nomenclature for the remainder of this manuscript. DFT calculations are presented in Fig. 1(g) where it can be visualized that multiple bands cross the Fermi level indicating YbTi_3Bi_4 to show metallic behavior. We further observe dispersionless bands at around 0.5 eV and 0.7 eV, indicating a high degree of localization of the corresponding electronic states. These dispersionless bands (see arrows), called flat bands from hereon, extend to a large part of the Brillouin zone. The bulk

band structure with the inclusion of SOC is presented in Fig. 1(h). As can be seen from the figure there is no significant effect on the presence of the flat bands with the inclusion of SOC.

To gain further insights into the contribution of different states, we have generated a band structure plot weighted by the band characters as presented in the supplementary information [53]. The flat bands observed at 0.5 eV, and 0.7 eV originate from the Ti d_{xy} and Ti $d_{x^2-y^2}$ orbitals, thus confirming their sole origination from the Ti kagome lattice. In addition to this, the flat band near the E_F and at the energy of around ~ 1.1 eV originate from the Yb^{2+} $4f$ orbital. This observation is also supported by the partial density of states (PDOS) plots as displayed in the supplementary information [53], which highlights the dominance of the Ti $3d$ states in the valence band region. The combination of band structure analysis and PDOS plots provides a comprehensive understanding of the electronic structure and its orbital character in YbTi_3Bi_4 .

To investigate the physical properties of YbTi_3Bi_4 , we grew high-quality single crystals using the flux method. The temperature-dependent molar magnetic susceptibility $\chi(T) = M/H$ measured at the magnetic field of $H = 0.1$ T is presented in Fig. 2(a) with $H \parallel c$ which reveals largely temperature-independent Pauli paramagnetism with a weak Curie tail from impurity spins. Extremely weak susceptibility (10^{-3} emu Oe $^{-1}$ mol $^{-1}$) is evident from Fig. 2(a) and we do not observe any signatures of bulk magnetic moments. We did not observe any qualitative difference when H is applied \parallel or \perp to the c -axis. The inset presents the magnetization as a function of magnetic field at selected temperatures of 300 K and 1.8 K which shows no saturation till the highest magnetic field of 7 T. Note that the scale of the M versus H plot is of the order of 10^{-2} μ_B per Yb, consistent with the polarization of impurity spins. The slight ferromagnetic impurity could either be from some Yb^{3+} , or other impurity elements.

In Fig. 2(b), we show the electrical resistivity ρ as a function of temperature when electric current is in the ab -plane where we can observe a typical metallic behavior till the lowest temperature of 2 K. The residual resistivity is approximately $20 \mu\Omega$ cm and the residual resistivity ratio is around 4. The fit to the resistivity data at low temperatures (< 80 K) is modeled via Fermi liquid behavior and a simple quadratic fit $\rho = \rho_0 + aT^2$ as can be seen by the red dotted line, where $\rho = 19.7 \mu\Omega$ cm and $a = 1.6 \times 10^{-3} \mu\Omega$ cm K $^{-2}$. We have also measured the specific heat (C_p) of the sample from 200 K down to 2 K without any magnetic field as presented in Fig. 2(c). We have fitted the C_p data to a limited temperature range from 2 K to 12 K using the Sommerfeld model. The total specific heat (C_p) for nonmagnetic metals is comprised of electronic C_e and lattice C_{ph} contributions. At low temperatures, the formula for the total specific heat is $C_p(T) = \gamma T + \beta T^3$ with $C_e = \gamma T$ and $C_{ph} = \beta T^3$. Here, γ is the Sommerfeld coefficient and $\beta = 12\pi^4 NR/5\Theta_D^3$

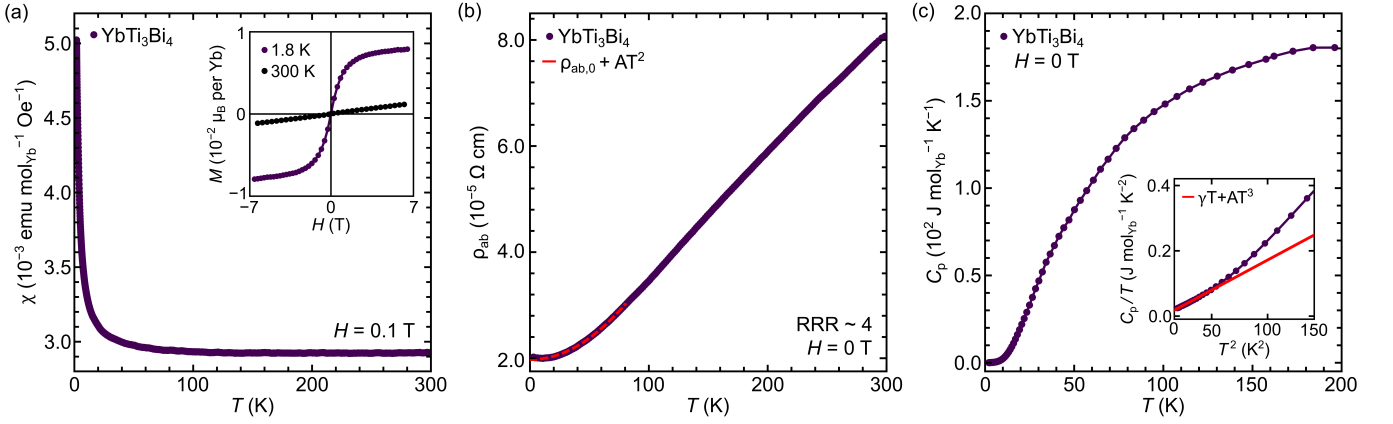


Fig. 2. Bulk electronic properties and single crystal characterization of YbTi_3Bi_4 . (a) Magnetic susceptibility (χ) vs temperature plot measured under a magnetic field of $H = 0.1$ T. The inset shows the magnetization as a function of magnetic field $M(H)$ measured up to 7 T for temperatures of 300 K and 1.8 K. (b) Temperature dependent zero-field electrical resistivity. (c) Temperature dependence of the specific heat (C_p) curve for temperatures 2-300 K. The lower inset displays C_p/T versus T^2 at low temperature.

with N , R , and Θ_D representing the number of atoms per unit cell, the ideal gas constant, and the Debye temperature, respectively. As can be seen in the inset of Fig. 2(c), the C_p/T scales linearly with T^2 at low temperatures. The resulting least-squares fit yields the parameters $\gamma = 1.78 \times 10^{-2} \text{ J mol}^{-1} \text{ K}^{-2}$ and $\beta = 1.46 \times 10^{-3} \text{ J mol}^{-1} \text{ K}^{-4}$. We do not observe any clear phase transitions from our measured magnetic, resistivity, or specific heat data which supports the classification of YbTi_3Bi_4 as a non-magnetic kagome metal and indicating Yb^{2+} rare-earth sublattice.

Next, we have performed ARPES measurements to understand the electronic structure of YbTi_3Bi_4 . At first, we initially focus on the Fermi surface (FS) topology. In Fig. 3(a), we have presented the Fermi surface (FS) map and constant energy contours (CECs) measured using a photon energy of 90 eV as a function of k_x and k_y and at various binding energies as noted on top of each plot. Several pockets can be seen at the Fermi level, with a circular pocket near the BZ center i.e, the $\bar{\Gamma}$ point, a distinct pocket with hexagonal symmetry which is anticipated due to the underlying symmetry of the kagome lattice along the $\bar{\Gamma}-\bar{M}$ direction and two pockets around the \bar{K} point, where the inner pocket seems to show a circular shape and the outer pocket is triangular. We note that the underlying structure is orthorhombic, which naturally imparts a small distortion to the kagome lattice. However, the distortion is minute, which results in the apparent 6-fold symmetry in the ARPES CEC data. We refer to the data using the hexagonal nomenclature, though there will be a slight underlying distortion that imparts 2-fold symmetry to the data. With the increase in binding energy the circular pocket at the $\bar{\Gamma}$ point contracts to a point-like feature at around ~ -370 meV. Below ~ -370 meV, this pocket starts to expand as can be seen from the CEC plot at ~ -520 meV, in-

dicating a Dirac-like state at the $\bar{\Gamma}$ point. The hexagonal pocket along $\bar{\Gamma}-\bar{M}$ direction decreases in size with increasing binding energy indicating its electron-like nature, whereas the triangular pocket at the \bar{K} point increases in size with increasing binding energy indicating its hole-like nature. Now, we turn our attention to the band dispersion along the $\bar{M}-\bar{\Gamma}-\bar{M}$ direction as shown in Fig. 3(b). In agreement with our measured FS and CECs, we observe electron-like pockets at the $\bar{\Gamma}$ and along the $\bar{\Gamma}-\bar{M}$ direction. Interestingly, the electron-like pocket at the $\bar{\Gamma}$ point shows a Dirac-like dispersion with Dirac node at around ~ -370 meV. This Dirac-like state is observed for photon energies from 100 eV to 70 eV as presented in Fig. 3(c). In addition to this, we observe hole-like pockets around the \bar{M} point. We can also observe the presence of multiple flat bands along the $\bar{M}-\bar{\Gamma}-\bar{M}$ direction. The flat bands around ~ 0.5 eV and ~ 0.7 eV can be visualized clearly which originates from the Ti $3d$ kagome planes as discussed in the earlier section.

To further examine the lack of dispersion of the flat bands, we have presented the band dispersion along the $\bar{\Gamma}-\bar{K}-\bar{M}-\bar{K}-\bar{\Gamma}$ high-symmetry direction using photon energies of 58 eV and 55 eV as presented in Fig. 4 (a) and Fig. 4(c), respectively. We can observe four dispersionless bands at the binding energies of 0.3 eV, 0.5 eV, 0.7 eV, and 1.1 eV for both the photon energies. The significant density of states (DOS) arising from the flat bands in YbTi_3Bi_4 can be further visualized by examining the momentum-integrated energy distribution curves (EDCs) as presented in Fig. 4(b) and Fig. 4(d), respectively. The EDCs as presented in Fig. 4(b,d) exhibits multiple distinct, sharp, and intense peaks which is indicated by black arrows. These peaks reflect the high DOS which is associated to the non-dispersive flat band in YbTi_3Bi_4 . In Fig. 4(e) and Fig. 4(f), we have presented the momentum-integrated EDCs as a function of

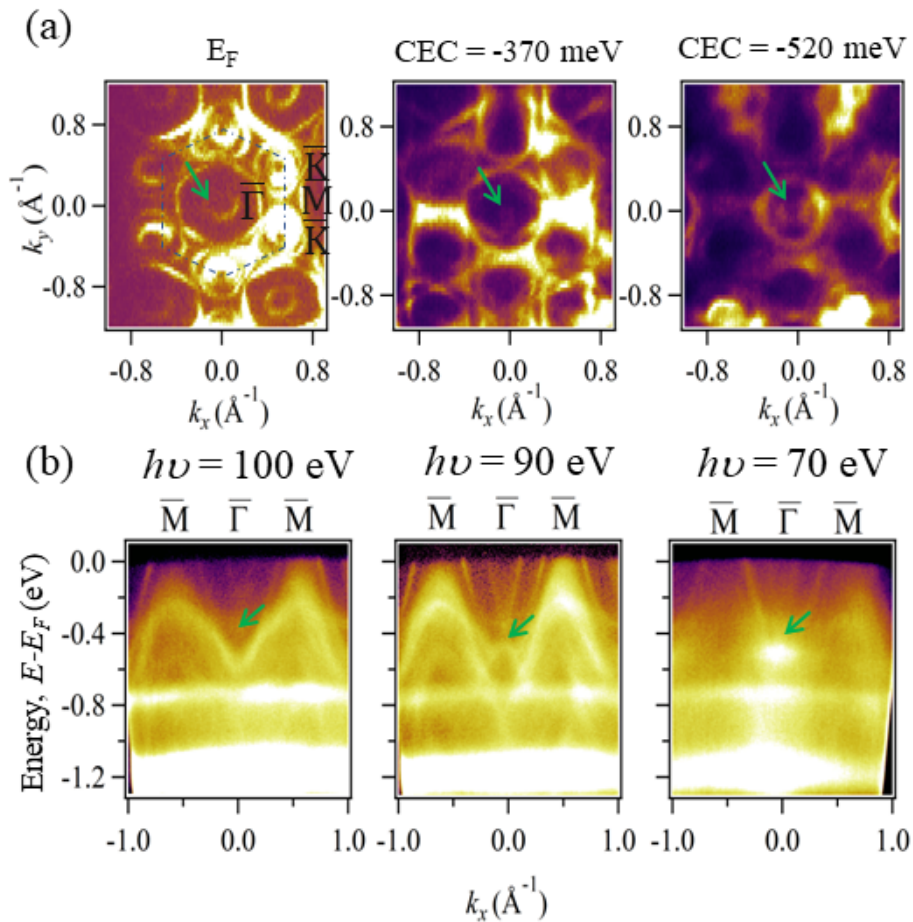


Fig. 3. Visualization of Dirac cones at the $\bar{\Gamma}$ point. (a) ARPES measured Fermi surface and constant energy contours at various binding energies as noted on top of each plot with a photon energy of 90 eV. High-symmetry points are labeled in black color. (b) Experimental band dispersion measured along the \bar{M} - $\bar{\Gamma}$ - \bar{M} high-symmetry direction with a photon energy of 100 eV, 90 eV, and 70 eV, respectively.

photon energies from 40 eV to 60 eV along both the \bar{K} - $\bar{\Gamma}$ - \bar{K} and $\bar{\Gamma}$ - \bar{K} - \bar{M} - \bar{K} - $\bar{\Gamma}$ high-symmetry directions. As can be seen clearly, the sharp intensity in the integrated DOS which originates from the flat bands as discussed above does not show any significant dispersion with the change in photon energies. Additional photon energy-dependent ARPES measured band dispersion [see Supplementary Information [53]] further reveal the dispersion of the flat bands does not change along the out-of-plane direction suggesting that the observed flat bands behave essentially as two-dimensional in nature.

Finally, we now turn our focus to the band dispersion along the \bar{K} - $\bar{\Gamma}$ - \bar{K} direction. At first, we discuss the band dispersion measured at a photon energy of 50 eV as presented in Fig. 5(a). From Fig. 5(a), we can see the presence of linear bands around the \bar{K} point. This band looks like a hole-pocket and seems to merge near the E_F . This band disperses from E_F till -0.3 eV and crosses the flat band. In addition to this, we also observe dispersive linear Dirac-like states at the $\bar{\Gamma}$ point, its intensity is however found to be reduced compared to Fig. 3(b) which may be due to the change in photoemission cross

section due to the change in photon energy. Apart from this two linear hole-like band can also be seen which disperses from -0.3 eV up to -1.2 eV. Next, we have repeated the same measurements but with different photon energies as presented in Fig. 5(b) and Fig. 5(c). We observe similar features as a function of photon energies. On a closer look we can see that the linear bands below -0.3 eV up to -1.2 eV show significant dispersion indicating its bulk origin. However, the linear band at the \bar{K} point does not seem to show significant dispersion. To further quantitatively analyze the dispersion of this linear Dirac-like band, we have presented the momentum-distribution curves integrated within a narrow energy range from the E_F till 5 meV below E_F as presented in Fig. 5(d). On tracking the dispersion of the band, we do observe slight dispersion of the band at the \bar{K} point indicating their quasi-two-dimensional nature. The state at the $\bar{\Gamma}$ however does not show significant dispersion within our experimental resolution in agreement with its surface state origin.

In summary, we have synthesized a novel nonmagnetic Ti based kagome material YbTi_3Bi_4 and comprehensively

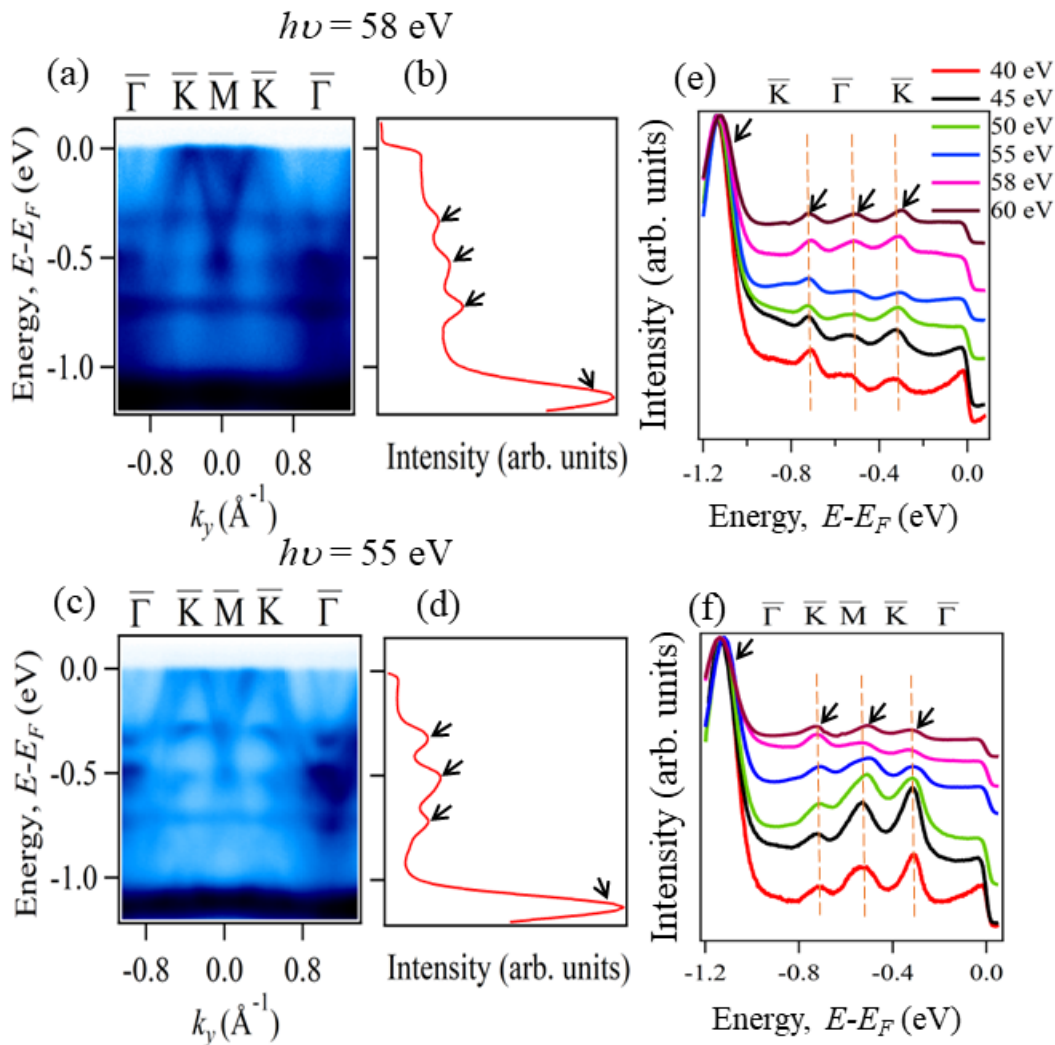


Fig. 4. Direct visualization of multiple flat bands along various high-symmetry directions. (a, b) Experimental band dispersion and integrated energy distribution curve (EDC) within the entire momentum range along the $\bar{\Gamma}$ - \bar{K} - \bar{M} - \bar{K} - $\bar{\Gamma}$ high-symmetry direction measured using a photon energy of 58 eV. The peak position of the EDCs, marked by black arrows, represent the flat bands. The flat bands are found to lie at ~ 0.3 eV, ~ 0.5 eV, ~ 0.7 eV with the most intense peak at around ~ 1.1 eV. (c, d) same as (a, b) but measured using a photon energy of 55 eV. (e) Integrated EDCs along the \bar{K} - $\bar{\Gamma}$ - \bar{K} high-symmetry direction within a momentum range of -0.8 \AA^{-1} to 0.8 \AA^{-1} . The EDCs have been taken at photon energies ranging from 40 eV to 60 eV as indicated in the figure. The peak position of the EDCs, marked by black arrows, represent the flat bands. (f) same as (e) but the integration is performed along the $\bar{\Gamma}$ - \bar{K} - \bar{M} - \bar{K} - $\bar{\Gamma}$ high-symmetry direction.

studied its detailed electronic structure using a combination of magneto-transport, ARPES, and DFT calculations. We have provided compelling evidence for the presence of multiple flat bands and topological Dirac states which originate from the Z_2 bulk topology. These flat bands originate from both the Ti based kagome lattice and $\text{Yb}^{2+}4f$ orbitals. Additionally, the presence of multiple flat bands offer an ideal environment to tune the chemical potential near the flat bands possibly by hole doping which can give rise to exotic physics such as ferromagnetism and superconductivity in these systems. Our work has uncovered crucial insights into the electronic structure of this material, which reveal another dimension in the studies of kagome based lattices and demon-

strate the importance of Ti based LnTi_3Bi_4 family as a potential platform to explore novel correlated, and topological phases. One can also tune the magnetism in these systems by replacing Yb with other rare earth elements. Our results would stimulate further studies to explore the interplay of magnetism, spin-orbit coupling, and topology in these new families of kagome materials.

Note added. Alongside this manuscript, several works were posted on arXiv within a short time period [46, 54–56].

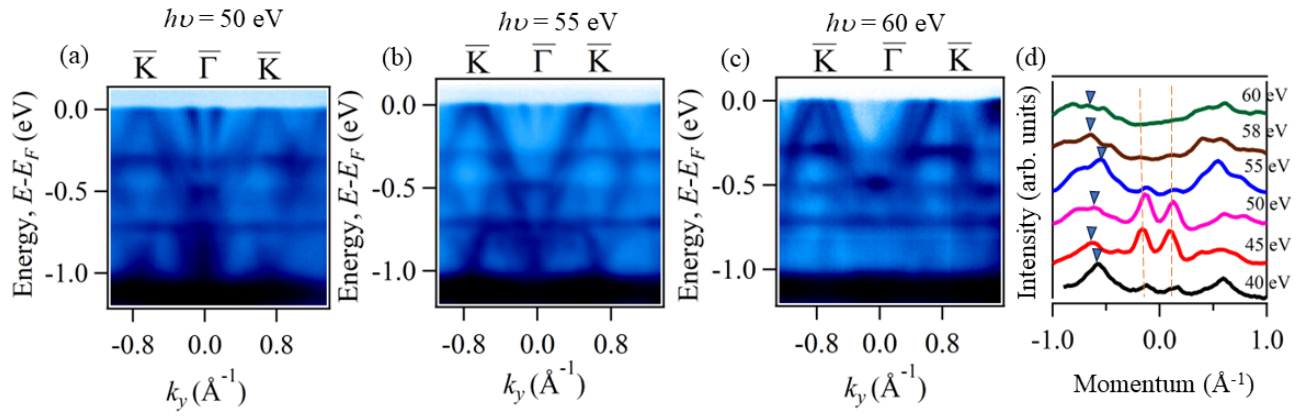


Fig. 5. Observation of Dirac state at the \bar{K} high-symmetry direction. Experimental band dispersion along the $\bar{K}-\bar{\Gamma}-\bar{K}$ high-symmetry direction measured using a photon energy of (a) 50 eV, (b) 55 eV, and (c) 60 eV, respectively. (d) Momentum distribution curves (MDCs) integrated within the energy window of 15 meV from the Fermi level. The MDCs are shown as a function of photon energy from 40 eV to 60 eV.

REFERENCES

- [1] I. Syózi, *Prog. Theor. Phys.* **6**, 306 (1951).
- [2] Y. Zhou, K. Kanoda, and T.-K. Ng, *Rev. Mod. Phys.* **89**, 025003 (2017).
- [3] T. Neupert, M. M. Denner, J.-X. Yin, R. Thomale, and M. Z. Hasan, *Nat. Phys.* **18**, 137 (2022).
- [4] H.-M. Guo and M. Franz, *Phys. Rev. B* **80**, 113102 (2009).
- [5] E. Tang, J.-W. Mei, and X.-G. Wen, *Phys. Rev. Lett.* **106**, 236802 (2011).
- [6] T.-H. Han, J. S. Helton, S. Chu, D. G. Nocera, J. A. Rodriguez-Rivera, C. Broholm, and Y. S. Lee, *Nature* **492**, 406 (2012).
- [7] L. Ye, M. Kang, J. Liu, F. von Cube, C. R. Wicker, T. Suzuki, C. Jozwiak, A. Bostwick, E. Rotenberg, D. C. Bell, L. Fu, R. Comin, and J. G. Checkelsky, *Nature* **555**, 638 (2018).
- [8] Z. Lin, J.-H. Choi, Q. Zhang, W. Qin, S. Yi, P. Wang, L. Li, Y. Wang, H. Zhang, and Z. Sun, *Phys. Rev. Lett.* **121**, 096401 (2018).
- [9] J.-X. Yin, S. S. Zhang, G. Chang, Q. Wang, S. S. Tsirkin, Z. Guguchia, B. Lian, H. Zhou, K. Jiang, I. Belopolski, N. Shumiya, D. Multer, M. Litskevich, T. A. Cochran, H. Lin, Z. Wang, T. Neupert, S. Jia, H. Lei, and M. Z. Hasan, *Nat. Phys.* **15**, 443 (2019).
- [10] J.-X. Yin, W. Ma, T. A. Cochran, X. Xu, S. S. Zhang, H.-J. Tien, N. Shumiya, G. Cheng, K. Jiang, B. Lian, Z. Song, G. Chang, I. Belopolski, D. Multer, M. Litskevich, Z.-J. Cheng, X. P. Yang, B. Swidler, H. Zhou, H. Lin, T. Neupert, Z. Wang, N. Yao, T.-R. Chang, S. Jia, and M. Z. Hasan, *Nature* **583**, 533 (2020).
- [11] M. Kang, L. Ye, S. Fang, J.-S. You, A. Levitan, M. Han, J. I. Facio, C. Jozwiak, A. Bostwick, and E. Rotenberg, *Nat. Mater.* **19**, 163 (2020).
- [12] M. Kang, S. Fang, L. Ye, H. C. Po, J. Denlinger, C. Jozwiak, A. Bostwick, E. Rotenberg, E. Kaxiras, and J. G. Checkelsky, *Nat. Commun.* **11**, 4004 (2020).
- [13] N. J. Ghimire and I. I. Mazin, *Nat. Mater.* **19**, 137 (2020).
- [14] M. Li, Q. Wang, G. Wang, Z. Yuan, W. Song, R. Lou, Z. Liu, Y. Huang, Z. Liu, H. Lei, Z. Yin, and S. Wang, *Nat. Commun.* **12**, 3129 (2021).
- [15] S. Regmi, T. Fernando, Y. Zhao, A. P. Sakhya, G. Dhakal, I. Bin Elius, H. Vazquez, J. D. Denlinger, J. Yang, and J.-H. Chu, *Commun. Mater.* **3**, 100 (2022).
- [16] J.-X. Yin, B. Lian, and M. Z. Hasan, *Nature* **612**, 647 (2022).
- [17] L. Balents, *Nature* **464**, 199 (2010).
- [18] J. Yang, X. Yi, Z. Zhao, Y. Xie, T. Miao, H. Luo, H. Chen, B. Liang, W. Zhu, Y. Ye, J.-Y. You, B. Gu, S. Zhang, F. Zhang, F. Yang, Z. Wang, Q. Peng, H. Mao, G. Liu, Z. Xu, H. Chen, H. Yang, G. Su, H. Gao, L. Zhao, and X. J. Zhou, *Nat. Commun.* **14**, 4089 (2023).
- [19] S. Nakatsuji, N. Kiyohara, and T. Higo, *Nature* **527**, 212 (2015).
- [20] A. K. Nayak, J. E. Fischer, Y. Sun, B. Yan, J. Karel, A. C. Komarek, C. Shekhar, N. Kumar, W. Schnelle, and J. Kübler, *Sci. Adv.* **2**, e1501870 (2016).
- [21] E. Liu, Y. Sun, N. Kumar, L. Muechler, A. Sun, L. Jiao, S.-Y. Yang, D. Liu, A. Liang, and Q. Xu, *Nat. Phys.* **14**, 1125 (2018).
- [22] D. F. Liu, A. J. Liang, E. K. Liu, Q. N. Xu, Y. W. Li, C. Chen, D. Pei, W. J. Shi, S. K. Mo, P. Dudin, T. Kim, C. Cacho, G. Li, Y. Sun, L. X. Yang, Z. K. Liu, S. S. P. Parkin, C. Felser, and Y. L. Chen, *Science* **365**, 1282 (2019).
- [23] W. Ma, X. Xu, J.-X. Yin, H. Yang, H. Zhou, Z.-J. Cheng, Y. Huang, Z. Qu, F. Wang, M. Z. Hasan, and S. Jia, *Phys. Rev. Lett.* **126**, 246602 (2021).
- [24] R. S. Li, T. Zhang, W. Ma, S. X. Xu, Q. Wu, L. Yue, S. J. Zhang, Q. M. Liu, Z. X. Wang, T. C. Hu, X. Y. Zhou, D. Wu, T. Dong, S. Jia, H. Weng, and N. L. Wang, *Phys. Rev. B* **107**, 045115 (2023).
- [25] X. Gu, C. Chen, W. S. Wei, L. L. Gao, J. Y. Liu, X. Du, D. Pei, J. S. Zhou, R. Z. Xu, Z. X. Yin, W. X. Zhao, Y. D. Li, C. Jozwiak, A. Bostwick, E. Rotenberg, D. Backes, L. S. I. Veiga, S. Dhési, T. Hesjedal, G. van der Laan, H. F. Du, W. J. Jiang, Y. P. Qi, G. Li, W. J. Shi, Z. K. Liu, Y. L. Chen, and L. X. Yang, *Phys. Rev. B* **105**, 155108 (2022).
- [26] T. Asaba, S. M. Thomas, M. Curtis, J. D. Thompson, E. D. Bauer, and F. Ronning, *Phys. Rev. B* **101**, 174415 (2020).
- [27] H. Zeng, G. Yu, X. Luo, C. Chen, C. Fang, S. Ma, Z.

- Mo, J. Shen, M. Yuan, and Z. Zhong, *J. Alloys Compd.* **899**, 163356 (2022).
- [28] N. J. Ghimire, R. L. Dally, L. Poudel, D. C. Jones, D. Michel, N. T. Magar, M. Bleuel, M. A. McGuire, J. S. Jiang, J. F. Mitchell, J. W. Lynn, and I. I. Mazin, *Sci. Adv.* **6**, eabe2680 (2020).
- [29] G. Dhakal, F. Cheenicode Kabeer, A. K. Pathak, F. Kabir, N. Poudel, R. Filippone, J. Casey, A. P. Sakhya, S. Regmi, C. Sims, K. Dimitri, P. Manfrinetti, K. Gofryk, P. M. Oppeneer, and M. Neupane, *Phys. Rev. B* **104**, L161115 (2021).
- [30] Q. Wang, K. J. Neubauer, C. Duan, Q. Yin, S. Fujitsu, H. Hosono, F. Ye, R. Zhang, S. Chi, K. Krycka, H. Lei, and P. Dai, *Phys. Rev. B* **103**, 014416 (2021).
- [31] F. Kabir, R. Filippone, G. Dhakal, Y. Lee, N. Poudel, J. Casey, A. P. Sakhya, S. Regmi, R. Smith, P. Manfrinetti, L. Ke, K. Gofryk, M. Neupane, and A. K. Pathak, *Phys. Rev. Mater.* **6**, 064404 (2022).
- [32] B. Lv, R. Zhong, X. Luo, S. Ma, C. Chen, S. Wang, Q. Luo, F. Gao, C. Fang, W. Ren, and Z. Zhong, *J. Alloys Compd.* **957**, 170356 (2023).
- [33] D. Chen, C. Le, C. Fu, H. Lin, W. Schnelle, Y. Sun, and C. Felser, *Phys. Rev. B* **103**, 144410 (2021).
- [34] B. R. Ortiz, L. C. Gomes, J. R. Morey, M. Winiarski, M. Bordelon, J. S. Mangum, I. W. Oswald, J. A. Rodriguez-Rivera, J. R. Neilson, and S. D. Wilson, *Phys. Rev. Mater.* **3**, 094407 (2019).
- [35] B. R. Ortiz, S. M. Teicher, Y. Hu, J. L. Zuo, P. M. Sarte, E. C. Schueller, A. M. Abeykoon, M. J. Krogstad, S. Rosenkranz, and R. Osborn, *Phys. Rev. Lett.* **125**, 247002 (2020).
- [36] B. R. Ortiz, P. M. Sarte, E. M. Kenney, M. J. Graf, S. M. Teicher, R. Seshadri, and S. D. Wilson, *Phys. Rev. Mater.* **5**, 034801 (2021).
- [37] B. R. Ortiz, S. M. L. Teicher, L. Kautzsch, P. M. Sarte, N. Ratcliff, J. Harter, J. P. C. Ruff, R. Seshadri, and S. D. Wilson, *Phys. Rev. X* **11**, 041030 (2021).
- [38] H. Zhao, H. Li, B. R. Ortiz, S. M. L. Teicher, T. Park, M. Ye, Z. Wang, L. Balents, S. D. Wilson, and I. Zeljkovic, *Nature* **599**, 216 (2021).
- [39] Y. Hu, X. Wu, B. R. Ortiz, X. Han, N. C. Plumb, S. D. Wilson, A. P. Schnyder, and M. Shi, *Phys. Rev. B* **106**, L241106 (2022).
- [40] Y.-X. Jiang, J.-X. Yin, M. M. Denner, N. Shumiya, B. R. Ortiz, G. Xu, Z. Guguchia, J. He, M. S. Hossain, X. Liu, J. Ruff, L. Kautzsch, S. S. Zhang, G. Chang, I. Belopolski, Q. Zhang, T. A. Cochran, D. Multer, M. Litskevich, Z.-J. Cheng, X. P. Yang, Z. Wang, R. Thomale, T. Neupert, S. D. Wilson, and M. Z. Hasan, *Nat. Mater.* **20**, 1353 (2021).
- [41] H. Zhao, H. Li, B. R. Ortiz, S. M. L. Teicher, T. Park, M. Ye, Z. Wang, L. Balents, S. D. Wilson, and I. Zeljkovic, *Phys. Rev. B* **106**, L081101 (2022).
- [42] Q. Yin, Z. Tu, C. Gong, Y. Fu, S. Yan, and H. Lei, *Chin. Phys. Lett.* **38**, 037403 (2021).
- [43] H. Luo, Q. Gao, H. Liu, Y. Gu, D. Wu, C. Yi, J. Jia, S. Wu, X. Luo, Y. Xu, L. Zhao, Q. Wang, H. Mao, G. Liu, Z. Zhu, Y. Shi, K. Jiang, J. Hu, Z. Xu, and X. J. Zhou, *Nat. Commun.* **13**, 273 (2022).
- [44] B. R. Ortiz, G. Pokharel, M. Gundayao, H. Li, F. Kaboudvand, L. Kautzsch, S. Sarker, J. P. C. Ruff, T. Hogan, S. J. G. Alvarado, P. M. Sarte, G. Wu, T. Braden, R. Seshadri, E. S. Toberer, I. Zeljkovic, and S. D. Wilson, *Phys. Rev. Mater.* **7**, 064201 (2023).
- [45] A. Ovchinnikov and S. Bobev, *Eur. J. Inorg. Chem.* **2018**, 1266 (2018).
- [46] B. R. Ortiz, H. Miao, F. Yang, E. M. Clements, D. S. Parker, J. Yan, A. F. May, and M. A. McGuire, *arXiv:2308.16138v1*, (2023).
- [47] P. C. Canfield, T. Kong, U. S. Kaluarachchi, and N. H. Jo, *Philos. Mag.* **96**, 84 (2016).
- [48] W. Kohn and L. J. Sham, *Phys. Rev.* **140**, A1133 (1965).
- [49] G. Kresse and J. Furthmüller, *Phys. Rev. B* **54**, 11169 (1996).
- [50] G. Kresse and D. Joubert, *Phys. Rev. B* **59**, 1758 (1999).
- [51] J. Sun, A. Ruzsinszky, and J. P. Perdew, *Phys. Rev. Lett.* **115**, 036402 (2015).
- [52] J. Sun, R. C. Remsing, Y. Zhang, Z. Sun, A. Ruzsinszky, H. Peng, Z. Yang, A. Paul, U. Waghmare, X. Wu, M. L. Klein, and J. P. Perdew, *Nat. Chem* **8**, 831 (2016).
- [53] See Supplemental Information for further details.
- [54] L. Chen, Y. Zhou, H. Zhang, X. Ji, K. Liao, Y. Ji, Y. Li, Z. Guo, X. Shen, and R. Yu, *arXiv preprint arXiv:2307.02942*, (2023).
- [55] J. Guo, L. Zhou, J. Ding, G. Qu, Z. Liu, Y. Du, H. Zhang, J. Li, Y. Zhang, and F. Zhou, *arXiv preprint arXiv:2308.14509*, (2023).
- [56] L. Chen, Y. Zhou, H. Zhang, Z. Guo, X. Yu, and G. Wang, *arXiv preprint arXiv:2308.14349*, (2023).

ACKNOWLEDGMENTS

M.N. acknowledges support from the Air Force Office of Scientific Research MURI (Grant No. FA9550-20-1-0322), the Air Force Office of Scientific Research under Award No. FA9550-17-1-0415, and the National Science Foundation (NSF) CAREER award DMR-1847962. Work performed by B.R.O. is sponsored by the Laboratory Directed Research and Development Program of Oak Ridge National Laboratory, managed by UT-Battelle, LLC, for the US Department of Energy. DGM acknowledge the support from AFOSR MURI (Novel Light-Matter Interactions in Topologically Non-Trivial Weyl Semimetal Structures and Systems), grant FA9550-20-1-0322. The work at Northeastern University was supported by the Air Force Office of Scientific Research under Award No. FA9550-20-1-0322, and it benefited from the computational resources of Northeastern University's Advanced Scientific Computation Center (ASCC) and the Discovery Cluster. This research used resources of the Advanced Light Source, a U.S. Department of Energy Office of Science User Facility, under Contract No. DE-AC02-05CH11231. We thank Sung-Kwan Mo and Jonathan Denlinger for beamline assistance at the Advanced Light Source (ALS), Lawrence Berkeley National Laboratory.